Green Chemistry

PAPER

View Article Online
View Journal | View Issue

Cite this: *Green Chem.*, 2026, **28**, 999

Unexpected magnesium oxide/calcium sulfide barnacle-like structures derived from pyrolysed carrageenans

Ewan D. Ward, Jolyon J. Glynn, Ryan E. Barker, Duncan J. Macquarrie and Avtar S. Matharu *

The production of unexpected magnesium oxide/calcium sulfide barnacle-like structures from pyrolysed carrageenan is reported. The pyrolysis of the precursor aerogel, sans dopants, activating agents, or templates, afforded sulfur-rich (3.9–7.6%) mesoporous chars (BJH P.V. 0.15–0.18 $cm^3\ g^{-1}$; 250–290 $m^2\ g^{-1}$). Carbothermic reduction of inherent sulfate salts yielded unique magnesium oxide/calcium sulfide barnacle-like structures (0.94 ± 0.34 μm diameter) decorating the char surface. Eruption of CO_2 in a volcano-like mechanism from MgO/CaS shells produced cavities affording barnacle-like structures. The chars at 800 °C (C800) were effective as copper(II) adsorbents (Q_e, 120 mg g^{-1}). Chemical precipitation of copper(II) hydroxy salts at barnacle sites exhibited pseudo-second order rate kinetics (k_2, 8.4 × 10–5 g $mg^{-1}\ min^{-1}$) and Freundlich adsorption characteristics (R^2, 0.894). These unique seaweed-derived materials potentially offer a sustainable solution to critical metal recovery.

Received 28th July 2025,
Accepted 7th November 2025

DOI: 10.1039/d5gc03892h

rsc.li/greenchem

Green foundation

1. Recognition of previously undescribed calcium sulfide/magnesium oxide barnacle-like structures derived from pyrolysed carrageenans, a renewable feedstock, which inherently contain sulfur, calcium and magnesium as opposed to sulfur, calcium and magnesium-doped materials. Based on thorough characterisation of the materials, a mechanism for the formation of these barnacle-like structures is given which mimics a volcanic-like expulsion of carbon dioxide from the calcium sulfide/magnesium oxide core.
2. The chars at 800 °C are effective as copper(II) adsorbents (Q_e, 120 mg g^{-1}). Chemical precipitation of copper(II) hydroxy salts at barnacle sites exhibited pseudo-second order rate kinetics (k_2, 8.4 × 10–5 g $mg^{-1}\ min^{-1}$) and Freundlich adsorption characteristics (R^2, 0.894).
3. These bespoke materials, unlike doped-materials, remediate copper but their future green chemistry reach, diversity and interest extends to recovery of globally topical critical metals using lower temperature derived chars.

Introduction

Metal oxide or sulfide nanoparticles have growing applications as supercapacitors,[1,2] adsorbents[3] and catalysts.[4] Nano and microscale metal oxides exhibit increased reactivity compared to bulk materials due to a higher density of crystalline edge and corner sites.[3] Magnesium is an abundant, environmentally benign mineral. Its oxide (MgO) nanoparticles have applications in CO_2 capture[5] and heavy metal adsorption.[3,6] Wei *et al.* and Zhou *et al.* reported magnesium oxide-loaded biochars as adsorbents for copper(II) remediation,[7,8] a critical metal. Decorated biochar materials are emerging materials in environmental remediation and decontamination.[9] Suspending nanoparticles within a porous carbon matrix offers an increased surface area for sorption and decreased diffusion distance for electron transfer.[2] The incorporation of MgO nanoparticles within char materials is often achieved by loading with magnesium chloride, obtained from the Dow process of seawater, and then calcinating.[3] Seaweed or macroalgal biomass naturally uptake minerals: magnesium, calcium, potassium, and sodium from their seawater habitat.[10] Salituro *et al.* reported the pyrolysis of seaweed kelp (*Laminaria hyperborea*) to afford biochars containing MgO nanoparticles,[5] enabling a one-pot synthesis of MgO containing biochars.

Many seaweeds contain an abundance of sulfated polysaccharides such as ulvans (Chlorophyta), fucoidans (Phaeophyta), agars or carrageenans (Rhodophyta).[11] Carrageenans, composed of β-galactose and 3,6-anhydro-α-galactose or α-galactose units, are desired as a gelling or rheology-altering agent in food and medicine.[12] The common forms of carrageenan (*iota* (ι), *kappa* (κ), and *lambda* (λ)) are distinguished by the position and quantity organosulfate func-

Green Chemistry Centre of Excellence, University of York, YO10 5DD, UK.
E-mail: avtar.matharu@york.ac.uk

tionalities.[12] Carrageenophytes (*Chondrus crispus*, *Mastocarpus stellatus*, *Kappaphycus alvarezii*, or *Eucheuma spinosum*) are abundantly distributed across global coastlines (British, Canadian, European, Chinese, Indonesian and Philippines)[13–15] and are often exploited for their fast production of carrageenan. Many extractable polysaccharides have been applied to environmental remediation, for example chitosan.[16] Carrageenan hydrogels and aerogels exhibit an affinity towards heavy metals that chelate with organosulfate functionalities and form metal–organic frameworks (MOF),[17] however, they lack the mechanical, thermal and chemical stability of carbons. Carrageenan-derived porous carbons are promising adsorbents due to their high surface area and mesoporous structure.[1,18] Nogueira *et al.* successfully adsorbed the antibiotic, ciprofloxacin, onto KOH activated carrageenan-derived porous carbons. The highly-graphitised material (2300 m^2 g^{-1}), enabled >99% removal of the antibiotic.[19] Carrageenan pyrolysis also reportedly affords sulfur-containing carbons (SCCs),[16,20] eliminating the need for toxic sulfur-based additives (sulfuric acid, hydrogen sulfide, thiophenes, or elemental sulfur) typically required for the synthesis of SCCs.[21] SCCs are often applied to heavy metal adsorption, Saka *et al.* produced sulfur-doped carbon particles *via* sulfuric acid functionalization of almond shell biochar, to remediate toxic cadmium (II).[22] Thus far, the prominent reported application for carrageenan-derived carbons is as metal sulfide-doped carbon aerogels for metal ion storage in electrode materials,[1] whereby the carbothermic reduction of deposited metal sulfate salts affords the corresponding metal sulfides.[23–25] Metal ion exchange at sulfate functional groups within the carrageenan MOF have therefore enabled selective metal sulfide content.[2,26] Mineral sulfides have also been recognized for their heavy-metal adsorption capacity.[27] Specifically, introducing calcium sulfate or sulfite to sawdust prior to pyrolysis yields calcium sulfide biochars with strong affinities for Ag, Cd, Pb, Cu, and Zn.[25]

Herein, we report the development of an efficient method for aqueous copper(II) adsorption by harnessing the inherent magnesium, calcium, and sulfur in unrefined hybrid κ/ι-carrageenan-based MOFs. Pyrolysis of this precursor, without the use of external reagents, yields unique magnesium oxide/calcium sulfide-decorated sulfur-containing porous carbons with an affinity to the critical metal, copper. The combined effect of inorganic MgO decoration and heteroatomic (nitrogen) doping on the adsorption of heavy metals or phosphates have been reported,[3,28,29] however, MgO/CaS-decorated sulfur-containing chars are unexplored as adsorbents. Irish Moss (*C. crispus*) carrageenan was subjected to pyrolysis at 250 °C, 400 °C, and 800 °C, without external dopants or activating agents. The resultant chars were characterised to determine their composition and surface properties. A noncompetitive adsorption approach was applied to determine the adsorption capacity of copper(II). Copper(II) adsorption was measured indirectly (UV-vis) and directly (pXRD, XPS and SEM-EDS analysis) and the adsorption kinetics and isotherms were produced *via* statistical analysis.

Results and discussion

MgO/CaS S-carbon adsorbent preparation and characterisation

Ground carrageenan aerogels (<50 μm) were hierarchically pyrolysed under reduced pressure and washed with hot water to remove excess salt content. The resultant wet chars were air-dried following solvent exchange with acetone. A detailed synthesis protocol and experimental characterisation are included in the SI. The final materials were labelled C*XXX* where *XXX* indicates pyrolysis temperature (°C).

Pyrolysis afforded brown (C250) to black (C800) powders (Fig. S1); consisting of reflective micro flakes (<200 μm diameter, 1–10 μm thick) (Fig. S2). Fig. 1a–d depicts the characterisation by SSNMR, FTIR, and XPS of C250–800 chars in comparison to the precursor carrageenan extract (IME). The rapid decomposition of pyranose structures (IME) into polymeric furfural-like structures (C250) is evident by a development of deshielded carbonyl and furanyl carbon environments in SSNMR (Fig. 1a) and coordinating carbonyl and olefinic stretching in FTIR (Fig. 1b). Further deoxygenation and decarboxylation enhance the degree of carbonization in C400 and C800, as evidenced by increased carbon content (Table S1), greater intensity of graphitic carbon states in XPS (Fig. 1c), and improved thermal stability in TGA (Fig. S3).[30] Progressive carbonization of IME to C800 results in a partial retention of precursor-derived sulfur, decreasing from 7.6 to 3.9 wt% (Table S1). A decrease in sulfur content was attributed to the deposition of metal sulfate salts, observed in the unwashed chars (Fig. S2 & S4), and subsequent removal during washes. Sulfur chemistry transitions were investigated *via* XPS (Fig. 1d) and indicated a reincorporation of inorganic sulfur into organic structures. Oxidation of alcohol/aldehyde functionalities to carboxyl (which are eventually removed by decarboxylation), likely enabled the reduction of organosulfate functionalities (IME) into sulfone or sulfonic acid in C250 and into thiol, thiophene, or disulfide in C400 and C800. These reduced sulfur states are commonly observed within sulfur-containing biochars in literature.[18,20] Incorporation of organosulfur within polyarene layers was visualised in C400 and C800 by the broad interlayer distance (0.39–0.41 nm) in TEM (Fig. S5) and corresponding 2θ values of the graphite (002) plane in pXRD (Fig. S6).

The lower carbon content of C800 materials (63%) in contrast to equivalent starch (S800: 92%) or alginic acid (A800: 81%) carbons reported in literature[31] is attributed to the mineral content (~4%, Table S1). Fig. 2a–e depicts the inorganic composites within C800. Magnesium oxide (MgO) and calcium sulfide (CaS) are generated within C800 evident by their characteristic cubic (200) and (220) planes in pXRD (Fig. 2a). Hydration of surface MgO to $Mg(OH)_2$ during washes was also observed by minor (001) and (101) diffraction planes in XRD; and FFT *d*-spacing of (101) and (102) planes in TEM (Fig. 2b). Visualisation of the inorganic content by SEM-EDS displayed barnacle-like hexagonal microcrystals (0.94 ± 0.34 μm diameter) containing a single cavity (200–300 nm diameter) decorating the char surface (Fig. 2c). Minimal evidence

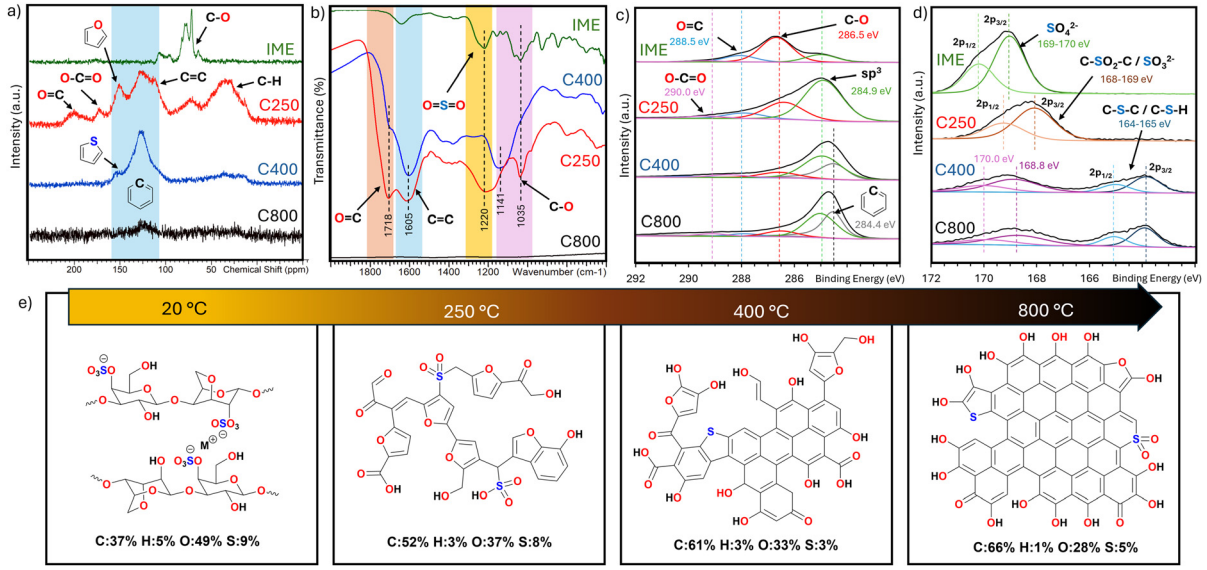

Fig. 1 . (a) ^{13}C CPMAS NMR spectra of IME and C250–C800; (b) FTIR spectra (600–2000 cm^{-1}) of (0.5%) C250–800 chars in KBr (Fig. S7); XPS spectra of IME and C250–C800 highlighting the (c) C 1s region (282–292 eV) and (d) S 2p region (172–162 eV); (e) schematic of the proposed C250–C800 char structures.

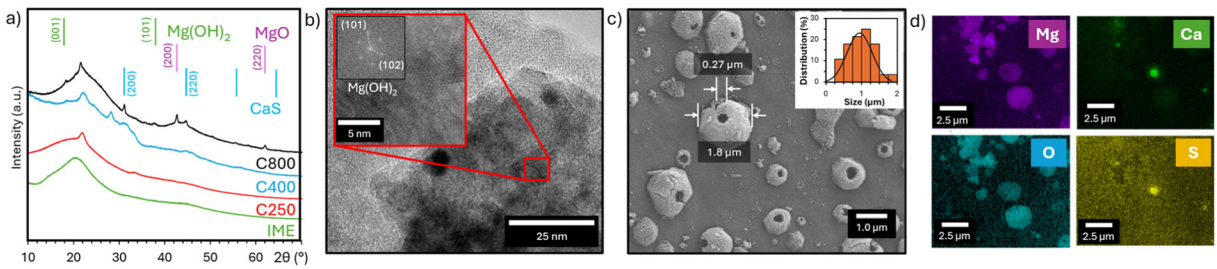

Fig. 2 (a) pXRD diffractogram of IME and C250–C800 highlighting MgO, CaS and $Mg(OH)_2$ diffraction planes; (b) HRTEM image at ×200k and ×500k (inset) magnification and FFT pattern of inorganic composites on C800; (c) SEM image at ×10k magnification and (d) SEM-EDS elemental mappings (Mg, Ca, O, and S) at ×5k magnification of barnacle-like structures.

of these structures being hollow was present in TEM imaging (Fig. S8) unlike many MgO microspheres.[32] Instead, these composites were composed of a shell of magnesium and oxygen and a solid core of calcium and sulfur (Fig. 2d).

Sulfates of magnesium, potassium, sodium and calcium develop from the material above 250 °C observed as hexagonal and needle-like crystals on the surface (Fig. 3a & b). ICP-MS of the carrageenan aerogel recognised these metals attributed to 4.5% of the materials dry weight (Table S1) which were accumulated from the biomass' natural environment.[10] MgO and CaS were formed above 700 °C (~1000 K) *via* the carbothermic reduction of deposited magnesium and calcium sulfates.[23,24] The endothermic nature of this reaction is evident in the DTG/DSC thermogram of the carrageenan precursor (Fig. S3). The carbothermic reduction of $MgSO_4$ and $CaSO_4$, shown in Fig. 3e, exhibits theoretical enthalpy changes ($\Delta H°$) of +177.8 and +159.0 kJ mol^{-1}, respectively, which are consistent with the DSC measurements.

The accumulation of magnesium and calcium as layered composites is not fully understood, however, a proposed mechanism of 'barnacle' formation is shown in Fig. 3e. The kinetics of $MgSO_4$ and $CaSO_4$ decomposition is unclear, however, Scheidema and Taskinen recognised a significant decrease in $MgSO_4$ decomposition temperatures alongside a reducing agent such as sulfur, carbon, or carbon monoxide (~600 °C)[33] compared to the carbothermic reduction of $CaSO_4$ (700 °C).[25] Therefore, we suggest an initial exergonic formation of an MgO shell from $MgSO_4$ (ΔG_{1000} = −91.4 kJ mol^{-1}) results in the encapsulation of a $CaSO_4$ core. Sequential carbothermic reduction of the core (ΔG_{1000} = −187.8 kJ mol^{-1}) generates CO and CO_2 and results in a volcano-like release of the evolved gases and formation of a cavity. Calcium sulfide encased in relatively insoluble $MgO/Mg(OH)_2$ was protected from dissolution,[34] whereas, remaining sodium and potassium sulfate salts and uncoated calcium sulfide (Fig. 3c) were aqueously removed (Fig. 3d).

The porous nature and surface chemistry of C250–C800 are shown in Fig. 4a–d. Mesoporous structures (BJH mesopore volume: 0.15–0.18 cm^3 g^{-1}) of high surface area (250–290 m^2 g^{-1} BET), associated carrageenan carbons,[35] were observed for

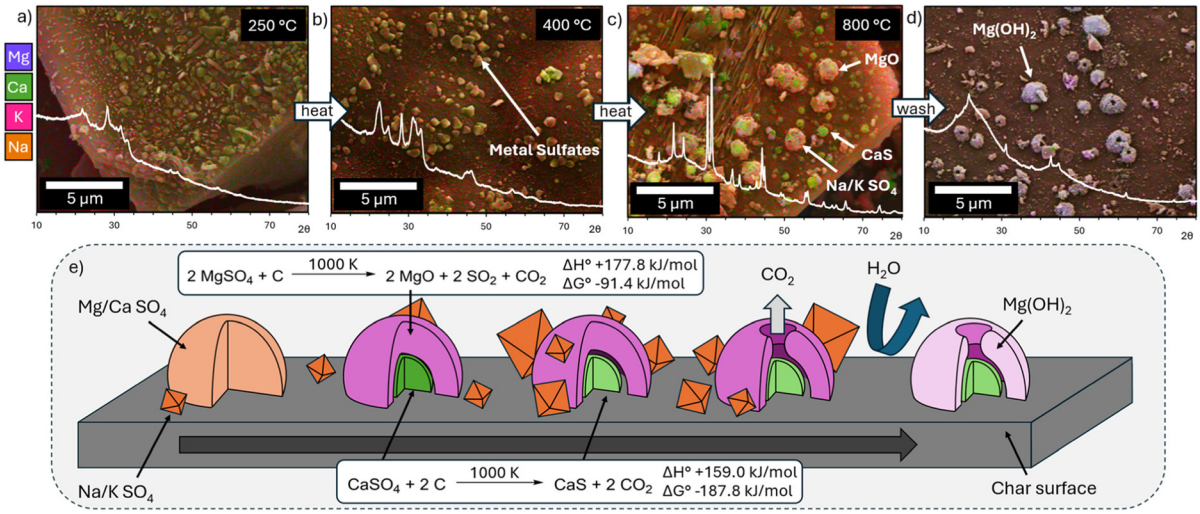

Fig. 3 Overlaid pXRD and SEM-EDS combined element maps of unwashed (a) C250, (b) C400, (c) C800, and (d) washed C800 at ×2.5k magnification; and (e) schematic representation of the 'barnacle' formation mechanism. Theoretical enthalpy changes and Gibbs free energy for reactions in (e) at 1000 K were determined according to I. Barin Thermochemical Data of Pure Substances.[36]

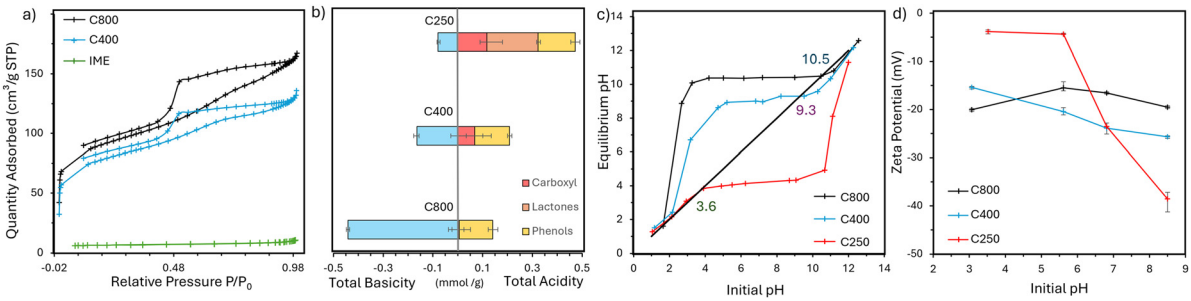

Fig. 4 (a) N_2 adsorption isotherms of IME aerogel, C400 and C800 chars (see Fig. S10 for C250); (b) Boehm titration acidity and basicity profiles; (c) point of zero charge pH plots; and (d) zeta potential titration for C250, C400 and C800 chars.

C400 and C800 by N_2 porosimetry (Table S2). The two materials were relatively indistinguishable by N_2 porosimetry measurements. Adsorption isotherms indicated capillary condensation in mesopores (Fig. 4a) and an average pore width (BJH) of ~5 nm was measured (Fig. S9). Low temperature pyrolysis (C250) afforded 'soft' structures susceptible to collapse and inconsistent N_2 porosimetry measurements (Fig. S10). TEM and SEM imaging (Fig. S11–13) of C250–C800 observed a predominantly macroporous (1–10 μm) structure within plate-like particles and mesopores (10–30 nm) were observed at higher magnifications in alignment with N_2 porosimetry.

A transition from surface acidity to basicity was measured from C250 to C800. High oxygen functionality within C250 affords acidic surfaces (0.47 ± 0.09 mmol g^{-1}) comprised of carboxyl (pK_a 3–6, 26%) and lactone-like (pK_a 7–9, 45%) acidity (Fig. 4b). Point-of-zero-charge (PZC) measurements (Fig. 4c) suggest anionic surfaces above pH 3.6, which is also observed in zeta potential measurements (−5 to −40 mV) (Fig. 4d). C400 and C800 materials, however, exhibit more basic surfaces attributed to fewer acidic functional groups and increase in graphitic functionality. Further, alkaline MgO/Mg$(OH)_2$ composites contribute to the highly basic surfaces of C800 (0.44 ± 0.007 mmol g^{-1}) *via* the uptake of H^+ to form Mg–OH^+.[8] Cationic surfaces below pH 10.5 are indicated by PZC measurements, although this contradicts with measured zeta potential values (−20 mV).

Copper(II) adsorption performance

As a valuable critical metal with applications in alloys, construction, electronics, and clean energy,[37] the demand for copper is increasing, especially with the uptake of clean technologies. The rapid turnover of electrical and electronic equipment produces significant quantities of waste (WEEE).[38] The production, use, and improper disposal of copper, often results in copper(II) ion presence within many industrial effluent streams[39] and electrical waste leachate.[40] Heavy metal pollution in soil and water systems is a current and growing global issue.[41–43] Copper remediation is essential due to the high toxicity of Cu^{2+} to human health and aquatic environ-

ments.[39] Adsorption is considered to be one of the most effective and cost efficient methods of pollutant removal.[44]

The performance of carrageenan carbons in the adsorption of copper(II) from aqueous solutions was investigated. Depicted in Fig. 5a, the effect of varying char dosage (1.0 mg mL^{-1} to 10.0 mg mL^{-1}) on the adsorption of copper(II) (c_0 5 g mL^{-1} $Cu(NO_3)_2$, pH_0 4, 24 h) revealed a maximum adsorption capacity (Q_e) of 120 mg g^{-1} was achieved by C800. Comparing the experimental Q_e values, C400 and C250 only achieved 67 and 54% of the adsorption performance of C800, respectively. Excluding the presence of MgO/CaS microstructures, C800 displayed similar chemical structure, porosity, and surface properties to C400. Acid washed C800 (C800A) materials exhibit high specific surface area (460 m^2 g^{-1} BET) (Table S2) without the presence of inorganic composites (Fig. S6). However, C800A exhibits significantly poorer adsorption capacity than C800 (Fig. 5a), which highlights the importance of MgO/CaS in the adsorption of copper(II) and indicates surface area has minor impact. Poor colloidal stability of these chars resulted in decreased Q_e values at higher doses. The sedimentation of char material inevitably reduces the surface area available for adsorption. This effect was more problematic in C400 and C800, due to fewer colloidal stabilising, ionisable or hydrophilic functional groups on the surface.

Copper(II) removal by C250–C800 was more effective at lower concentrations of copper(II). At higher concentrations (1.7 g L^{-1}), copper(II) removal is less effective (10–30%) due to surface saturation (Fig. S14). Fig. 5b depicts the effect of contact time on copper(II) removal (%) from 0.2 g L^{-1} copper (II) solutions. 84% removal was achieved by C800 and 57% and 61% for C250 and C400, respectively. The removal of copper(II) ions aligns well with the adsorption capacities of these materials. Competition between H^+ and Cu^{2+} for anionic adsorption sites result in pH shifts during adsorption. The pH was monitored by probe to visualise the effect of adsorption and copper removal on pH (Fig. 5b). C800 and C400 materials experienced an increase in pH to 5.0 and 4.5, respectively. This decrease in H^+ concentration may be attributed to neutralisation of alkaline sites on the surface of these chars or the formation of Mg–OH^+ discussed above and the removal of acidic Cu^{2+}. The increased copper(II) removal using C800 consequently affords more neutral pH solutions at equilibrium than C400. Conversely, C250 materials exhibit a decrease in pH to 2.6, which indicates the adsorption of copper(II) onto C250 involves an exchange at protonated sites, such as carboxyl, phenol, or thiol functionalities and the release of H^+ into solution.

The influence of the initial pH of the copper(II) solution on the equilibrium adsorption capacity is shown in Fig. 5c. The enhance affinity for copper(II) of C800 reduces rapidly from approximately 80 to 20 mg g^{-1} between pH 4.5 and 2.0, respectively. This is due to increased competition between protons and metal ions in solution consistent with literature.[45] The most drastic decrease between pH 3 and 2 also aligns with the acidity in which C800 ceases to buffer the pH (Fig. 5d). C400 exhibits a similar trend in adsorption capacity and behaves almost identically to C800 below pH 2. Interestingly, all three materials exhibit an increase in adsorption capacity at

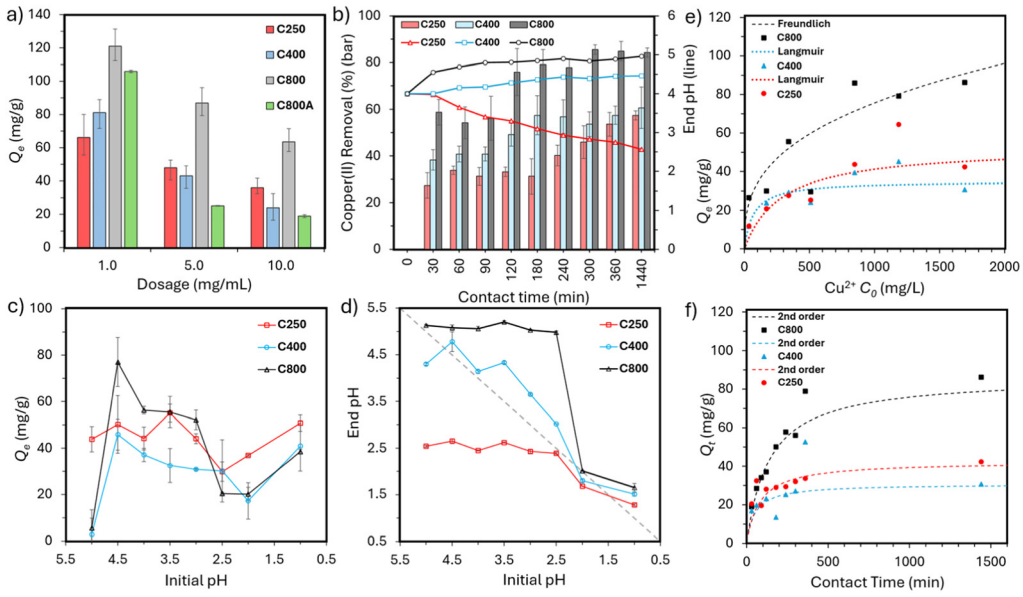

Fig. 5 (a) Copper(II) adsorption capacity (Q_e) of C250–800 chars at variable doses (1.0–10.0 mg mL^{-1}) from aqueous copper(II) nitrate (Cu^{2+} c_0 1.7 g mL^{-1}, pH_0 4.0, 25 °C, 24 h); (b) effect of C250–800 char (5.0 mg L^{-1}) contact time on copper(II) removal (%) from solution (Cu^{2+} c_0 0.2 g L^{-1}, pH_0 4.0, 25 °C) (bar) and measured pH (line); (c) effect of initial pH of the copper(II) nitrate solution (Cu^{2+} c_0 1.3 g mL^{-1}, 25 °C, 24 h) on the adsorption capacity (Q_e) of C250–800 chars (5.0 mg L^{-1}) and (d) the equilibrium (end) pH of the solution; (e) copper(II) adsorption isotherms (pH_0 4.0, 25 °C, 24 h) for C250–800 chars (5.0 mg L^{-1}) and the corresponding Freundlich or Langmuir isotherm model fitting; (f) copper(II) adsorption kinetics (Cu^{2+} c_0 1.7 mg mL^{-1}, pH_0 4.0, 25 °C) for C250–800 chars (5.0 mg L^{-1}) and the corresponding pseudo-2nd order model fittings (isotherm and kinetic parameters, fitting, and errors are available in Tables S3 and S4, respectively).

pH 1; however, the underlying cause remains unclear, as electrostatic adsorption is unlikely at this pH. The increased nitric acid concentration may promote oxidation of surface thiol or sulfide groups to sulfoxide or sulfone species, thereby enhancing adsorption capacity through the generation of additional active sites. In future, XPS analysis of the acidified char would provide clarification. Under weakly acidic conditions (pH 5.0), C800 and C400 exhibit limited copper(II) adsorption capacities, attributable to copper speciation and the predominance of $CuOH^+$ species that interact weakly with adsorption sites.

The adsorption capacity (Q_e) as a function of the initial copper(II) concentration (c_0) is shown in Fig. 5e. The experimental data was fitted to Freundlich and Langmuir adsorption isotherm models using linear regression analysis (Fig. S15) and the goodness of fit assessed (Table S3). C800 materials correlated well with Freundlich modelling (R^2 = 0.894), suggesting the adsorption of copper(II) to these surfaces has multilayer adsorption characteristics and the materials exhibit heterogeneous adsorption sites.[46] C250 and C400, however, correlated better to Langmuir models (R^2 = 0.876–0.927) indicating monolayer adsorption characteristics and homogeneous adsorption sites.[47] The kinetics of adsorption were investigated by assessing the copper(II) adsorption capacity against contact time (Fig. 5f). The maximum adsorption capacity for each char was met within 480 min under these conditions. The kinetic data was fitted to pseudo-first and pseudo-second order models (Fig. S16) which assume the rate-limiting step of adsorption is the interaction between adsorbate and adsorbent.[48] The fitting was assessed as above (Table S4) and adsorption onto C250–C800 correlate well with pseudo-second order models (R^2 = 0.952–0.999), which suggests chemisorption of copper(II) is the rate-limiting step.[48] C400 also correlated well with pseudo-first order models (R^2 = 0.975) which could suggest physisorption involvement. The calculated pseudo-second order rate constant followed the trend C400 > C250 > C800. Adsorption onto MgO typically exhibits a slower rate in literature, which is explained by the positive charge formed at MgO sites (Mg–OH^+) and electrostatic repulsion of copper(II) ions.[8]

Post-copper(II) adsorption characterisation

Dry copper(II)-adsorbed chars (Cu-C*XXX*) (pH_0 4.0, c_0 1.7 g L^{-1}, 25 °C, 24 h, dosage 5.0 mg mL^{-1}) were analysed by XPS, pXRD and SEM-EDS, depicted in Fig. 6a–g, to recognise copper uptake by C250–C800. XPS analysis (Fig. 6a) identified copper 3p, 3s, 2p, and auger spectral lines within all three materials. Integration of the $2p_{3/2}$ region (935–945 eV), recognised a maximum copper content in C800 (12%), followed by C400 (3%) and C250 (1%) chars. Deconvolution of copper $2p_{3/2}$ spectral region indicated the presence of reduced Cu(I) or Cu(0) in all three chars (Fig. S17), which could suggest a redox adsorption mechanism. However, copper is susceptible to reduction during XPS analysis and it is therefore unclear whether reduction occurred during adsorption.

The copper content estimated from the average intensity of Cu 0.9, 8.0 and 8.9 eV X-ray lines in SEM-EDS spectra indicated a reverse trend to XPS (Fig. 6e–g). Unlike Cu-C250 and Cu-C400, Cu-C800 copper content was not homogeneously dispersed across the surface, in alignment with adsorption iso-

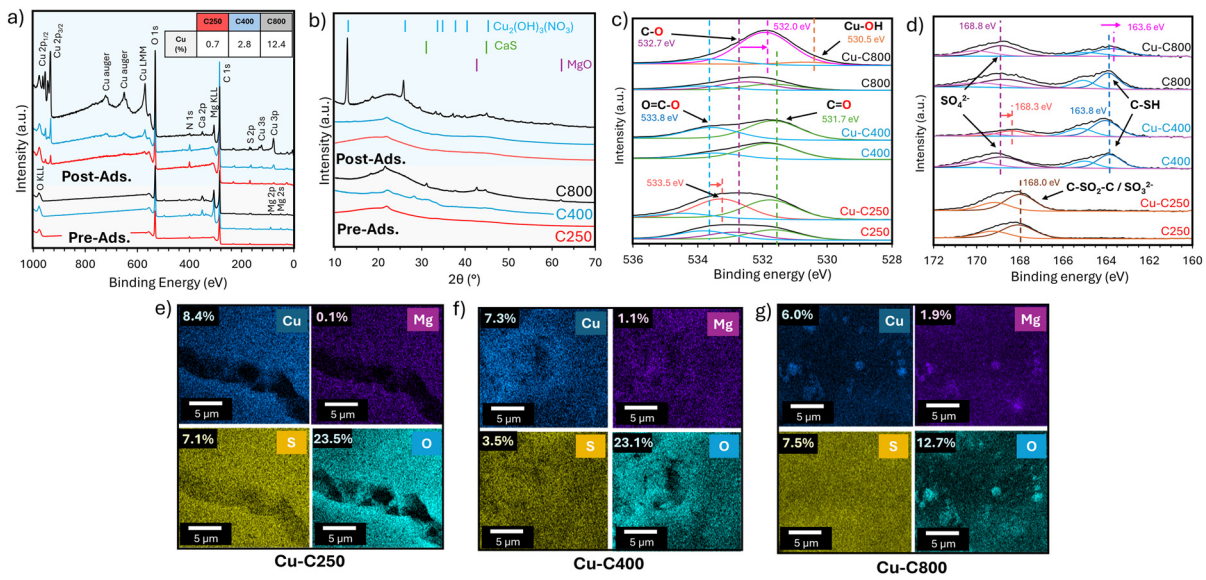

Fig. 6 (a) XPS spectra of C250–800 and Cu-C250–800 (pH_0 4.0, c_0 1.7 g L^{-1}, 25 °C, 24 h, dosage 5.0 mg mL^{-1}) (tabulated copper $2p_{3/2}$ content (%) inset); (b) XRD diffractograms of C250–800 and Cu-C250–800 (pH_0 4.0, c_0 1.7 g L^{-1}, 25 °C, 24 h, dosage 5.0 mg mL^{-1}); (c) O 1s region (528–236 eV) and (d) S 2p region (162–172 eV) XPS spectra of C250–800 and Cu-C250–800; SEM-EDS element maps (Cu. Mg, S, O) for (c) Cu-C250, (d) Cu-C400, and (e) Cu-C800 chars (pH_0 4.0, c_0 1.7 g L^{-1}, 25 °C, 24 h, dosage 5.0 mg mL^{-1}).

therm modelling. In Cu-C800 the copper adsorbate was concurrent with magnesium and oxygen (Fig. 6g), indicating adsorption at magnesium oxide barnacle sites. Furthermore, pXRD (Fig. 6b) displayed (001) and (002) reflexes at 12.8° and 25.8°, respectively, associated with copper(II) hydroxy nitrate ($Cu_2(OH)_3NO_3$).[3,49] Copper(II) hydroxy nitrate presence offers potential catalytic applications of the afforded copper-adsorbed C800. Amaniampong *et al.* demonstrated that sonication of copper(II) hydroxy nitrate in water produces a copper oxide catalyst effective for glycerol oxidation to dicarboxylic acids.[50] Chemical precipitation of $Cu_2(OH)_3NO_3$ has been reported as an adsorption mechanism of copper(II) onto MgO loaded materials.[8,49] Electrostatic layering: $Mg–OH^+ \leftrightarrow Mg–OH^+–NO_3^- \leftrightarrow Mg–OH^+–NO_3^-–Cu^{2+}$ initiates copper(II) hydroxy nitrate crystallisation at MgO sites.[8] Magnesium hydroxide has been reported to achieve similar results by providing a site for ion-exchange.[51] This mechanism is supported by the loss in the $Mg(OH)_2$, MgO and CaS diffraction patterns in Cu-C800 (Fig. 6b) similarly observed by Ling *et al.*[3] These chemisorption-based mechanisms supports kinetic modelling (pseudo-second order) and the formation of salts is in alignment with a multilayer adsorption isotherm (Freundlich).

XRD analysis of chars following adsorption at varying acidity (Fig. S18) recognised decreasing intensities of the (001) and (002) reflexes of copper(II) hydroxy nitrate from pH 4.5 to 2.5, attributable to proton interference within electrostatic layering. At pH 5.0 surface oxygen sites on MgO ($Mg–OH^+$) undergo partial deprotonation[52] which also results in a decrease in adsorbed copper content on the surface.

Fig. 6c shows the XPS O 1s region of copper(II)-adsorbed C250–800. In C250–800, a broad signal composed of peaks at 533.8, 532.7, and 531.7 eV are associated with O=C–O, C–O, and C=O functionalities, respectively, and correlates with the C 1s 286, 287, and 289 eV peaks (Fig. 1b). Metal oxide O 1s peaks (~530 eV) are not visible in C800, this is attributed to surface oxide hydration to hydroxide (~532 eV).[53] After adsorption the O 1s region exhibits increased intensity around 530–531 eV associated with Cu–OH.[54,55]

Decreases in binding energy (red shift) of O 1s peaks following adsorption indicate an increase in electron density at the oxygen atom associated with binding to a less electronegative atom; *i.e.* copper (χ_r 1.9) over hydrogen (χ_r 2.2). Alongside adsorption at MgO sites, C800 exhibits adsorption at phenolic functionality, noticeable by red shifts in the C–O O 1s peak (532.7 eV) to 532.0 eV. In C250, a red shift in carboxyl oxygen states afforded a peak at 533.5 eV suggesting copper chelation. This binding to carboxyl functional groups correlates with a decrease in pH (Fig. 5b). The XPS S 2p region of the copper(II)-adsorbed C250–800 is shown in Fig. 5d. Cu-C250 exhibited little to no change in sulfur state suggesting the sulfonic acid or sulfone functionalities are surprisingly not involved in adsorption. Cu-C800 materials exhibit a minor shift in the thiol-like 2p peak (163.8 eV) to 163.6 eV. This could indicate copper(II) binding, however, in previous reports metal binding to thiol or disulfides exhibit much greater shifts to ~162 eV.[56] Cu-C400 chars exhibit a clear reduction in intensity of sulfate-like sulfur state peak (168.8 eV) attributed to the dissolution of trapped or recalcitrant sulfate salts. Evident by the decrease in crystallinity of this material in pXRD (Fig. 6b). Shifts in the remaining S 2p region and O 1s regions of this material have not been observed, which could indicate physisorption is key in the adsorption of copper(II) onto C400 in alignment with kinetic studies.

Experimental

Preparation of MgO/S carrageenan carbons

Hybrid κ/ι-carrageenan aerogel obtained from Irish Moss biomass (SI) (10 g) was loaded into a quartz flask, placed under vacuum (~30 mbar), and heated within a Barnstead 6000 Muffle Furnace using the following program: heat to 100 °C (5 °C min^{-1}) and held for 60 min. Further heating to 400 °C (0.3 °C min^{-1}) proceeded, followed by additional heating to 800 °C (2 °C min^{-1}). C*XXX* samples were isothermally heated at *XXX* °C (*XXX* equated to either 250, 400, or 800) for 30 minutes prior to collection and subsequent washing with hot water (100 mL) for 1 h. Filtered and rinsed (2 × 50 mL hot water) chars were finally washed with acetone (50 mL) and air dried (yield: C250 = 61.0 ± 1.2%, C400 = 48.1 ± 0.2%, C800 = 29.4 ± 1.2%).

Copper(II) adsorption studies

The adsorption performance of MgO/CaS char materials were determined by suspending test material (10–100 mg) in aqueous copper(II) nitrate solutions (10 mL, 100–5000 mg L^{-1}) and agitating in a shaking water bath (25 °C) for 24 h. For pH studies copper(II) solution acidity was adjusted by dissolving copper(II) nitrate in solutions of nitric acid (pH 5.0–1.0). The equilibrium pH (Jenway model 6505) and UV-vis absorbance spectrum (900–400 nm) of the filtered copper(II) solution was then measured and the copper(II) concentration was determined by calibration curve (λ_{max} 810 nm) (SI). The adsorption capacity was then determined *via* eqn (1) and copper(II) removal by eqn (2):

$$q_e = \frac{V(c_0 - c_e)}{m} \quad (1)$$

$$\text{Cu(II) removal}\,\% = \frac{(c_0 - c_e)}{c_0} \times 100\% \quad (2)$$

where q_e is the equilibrium adsorption capacity (mg g^{-1}), V is the volume (L), c_0 is the initial concentration (mg L^{-1}), c_e is the equilibrium concentration (mg L^{-1}), and m is the mass of adsorbent (g). Adsorption isotherm and kinetic models were applied using linear regression analysis described in the SI.

The residue testing materials from the copper(II) adsorption experiments were collected and washed with distilled water and acetone before air-drying. These samples were labelled Cu-C*XXX* (where *XXX* indicates pyrolysis temperature) and then analysed by pXRD, XPS and SEM-EDS (SI).

Conclusions

The promising results of this study should invoke further development of inherent MgO/CaS-decorated sulfur-containing porous carbons derived from seaweed for critical metal recovery from waste streams. The high surface area and mesoporous structure is abundant with both organic and inorganic active adsorption sites. The results demonstrated that magnesium oxide decoration increased copper(II) adsorption performance (120 mg g^{-1}) over sulfur incorporation alone (65–80 mg g^{-1}). Contrasting ethylene glycol/urea-grown flower-like MgO microspheres reported in literature,[49] these novel barnacle structures exhibit 1/4 of the adsorption capacity but use 30 times less magnesium, indicating that the dispersion of MgO over a sustainably derived porous matrix delivers a higher efficiency. Furthermore, the fabrication of these chars using green processes incorporates inherent sulfur and mineral content of this renewable seaweed resource and eliminates the need for external dopants or templates. In future work, the addition of a competitive adsorption study and recycle test should be performed to determine the material selectivity and reusability, respectively. This would provide valuable information for the real-world application of these materials to critical metal recovery from WEEE leachate.

Author contributions

Conceptualisation, E. D. W. & A. S. M.; methodology & investigation, E. D. W., J. J. G., R. E. B. & A. S. M.; writing (original draft), E. D. W.; writing (review & editing), E. D. W., D. M. & A. S. M.; supervision, A. S. M. All authors have read and agreed to the published version of the manuscript.

Conflicts of interest

The authors declare no conflict of interests.

Data availability

The data supporting this article have been included as part of the supplementary information (SI). Supplementary information is available. Detailed experimental procedures and supplementary figures. See DOI: https://doi.org/10.1039/d5gc03892h.

Acknowledgements

From the University of York Green Chemistry Centre of Excellence, we would like to thank Suranjana Bose and Richard Gammons for their expert technical support, Graeme McAllister for providing CHNS analysis. From the Biorenewables Development Centre (BDC), York, we thank Jon Angus for providing ICP-MS analysis. From the University of Liverpool, and from the University of Cardiff, David J. Morgan for providing XPS analysis.

References

1 W. Wei, Y. Zheng, M. Huang, J. Shi, L. Li, Z. Shi, S. Liu and H. Wang, *Nanoscale*, 2021, **13**, 4911–4920, DOI: 10.1039/D0NR09011E.
2 D. Li, Y. Sun, S. Chen, J. Yao, Y. Zhang, Y. Xia and D. Yang, *ACS Appl. Mater. Interfaces*, 2018, **10**, 17175–17182, DOI: 10.1021/acsami.8b03059.
3 L.-L. Ling, W.-J. Liu, S. Zhang and H. Jiang, *Environ. Sci. Technol.*, 2017, **51**, 10081–10089, DOI: 10.1021/acs.est.7b02382.
4 J. Kaur, K. Kaur, S. K. Mehta and A. S. Matharu, *J. Mater. Chem. A*, 2020, **8**, 14519–14527, DOI: 10.1039/D0TA05388K.
5 A. Salituro, A. Westwood, A. Ross and R. Brydson, *Sustainable Chem.*, 2020, **1**, 33–48, DOI: 10.3390/suschem1010003.
6 Y. Xu, H. Xia, Q. Zhang, G. Jiang, W. Cai and W. Hu, *Arabian J. Chem.*, 2022, **15**, 104059, DOI: 10.1016/j.arabjc.2022.104059.
7 Y. Wei, T. Chen, Z. Qiu, H. Liu, Y. Xia, Z. Wang, R. Zou and C. Liu, *Bioresour. Technol.*, 2022, **365**, 128146, DOI: 10.1016/j.biortech.2022.128146.
8 Y. Zhou, X. Wang, Y. Yang, L. Jiang, X. Wang, Y. Tang and L. Xiao, *Environ. Res.*, 2024, **251**(2), 118652, DOI: 10.1016/j.envres.2024.118652.
9 H. Zhou, R. Zhang, C. Yue, X. Wu, Q. Yan, H. Wang, H. Zhang and T. Ma, *Chin. J. Catal.*, 2024, **59**, 169–184, DOI: 10.1016/S1872-2067(23)64613-3.
10 A. B. Ross, C. Hall, K. Anastasakis, A. Westwood, J. M. Jones and R. J. Crewe, *J. Anal. Appl. Pyrolysis*, 2011, **91**, 344–351, DOI: 10.1016/j.jaap.2011.03.012.
11 J. Muthukumar, R. Chidambaram and S. Sukumaran, *J. Food Sci. Technol.*, 2021, **58**, 2453–2466, DOI: 10.1007/s13197-020-04837-0.
12 K. Alba and V. Kontogiorgos, in *Encyclopedia of Food Chemistry*, ed. L. Melton, F. Shahidi and P. Varelis, Elsevier, Oxford, 2019, pp. 240–250.
13 J. Collén, M. L. Cornish, J. Craigie, E. Ficko-Blean, C. Hervé, S. A. Krueger-Hadfield, C. Leblanc, G. Michel, P. Potin, T. Tonon and C. Boyen, in *Advances in Botanical Research*, ed. N. Bourgougnon, Elsevier, 2014, vol. 71, pp. 53–89.
14 J. Zhang, S. Waldron, Z. Langford, B. Julianto and A. M. Komarek, *J. Appl. Phycol.*, 2023, **36**, 1–22, DOI: 10.1007/s10811-023-03004-0.
15 L. Pereira and F. van de Velde, *Carbohydr. Polym.*, 2011, **84**, 614–623, DOI: 10.1016/j.carbpol.2010.12.036.
16 Y. Zhou, Y. Zhang, Y. Nie, D. Sun, D. Wu, L. Ban, H. Zhang, S. Yang, J. Chen, H. Du and X. Pan, *Prog. Mater. Sci.*, 2025, **152**, 101460, DOI: 10.1016/j.pmatsci.2025.101460.
17 H. Ghasemzadeh, S. Shidrang and A. K. Vanashi, *Int. J. Biol. Macromol.*, 2024, **292**, 139164, DOI: 10.1016/j.ijbiomac.2024.139164.

18 X. Chen, L. Zhang, W. Xu, X. Ding, S. Chen, X. She, X. Guo, C.-L. Dong, Y. Huang, L. Zhang, S. Shen and D. Yang, *Appl. Catal., B*, 2022, **313**, 121425, DOI: 10.1016/j.apcatb.2022.121425.
19 J. Nogueira, M. António, S. M. Mikhalev, S. Fateixa, T. Trindade and A. L. Daniel-da-Silva, *Nanomaterials*, 2018, **8**, 1004, DOI: 10.3390/nano8121004.
20 N. Garland, R. Gordon, I. Hopkins, E. Ward, C. R. McElroy, D. MacQuarrie and A. Parkin, *Carbon*, 2025, **239**, 120309, DOI: 10.1016/j.carbon.2025.120309.
21 W. Kiciński, M. Szala and M. Bystrzejewski, *Carbon*, 2014, **68**, 1–32, DOI: 10.1016/j.carbon.2013.11.004.
22 C. Saka, İ. Teğin and K. Kahvecioğlu, *Diamond Relat. Mater.*, 2023, **131**, 109542, DOI: 10.1016/j.diamond.2022.109542.
23 B. Souza, R. Souza, I. Santos and E. Brocchi, *J. Mater. Res. Technol.*, 2020, **9**, 1847–1855, DOI: 10.1016/j.jmrt.2019.12.017.
24 X. Jia, Q. Wang, L. Han, L. Cheng, M. Fang, Z. Luo and K. Cen, *J. Anal. Appl. Pyrolysis*, 2017, **124**, 319–326, DOI: 10.1016/j.jaap.2017.01.016.
25 Y. Lu, Q. Wang, F. Yu, S. Zhang and X. Zhu, *Carbon Res.*, 2023, **2**, 5, DOI: 10.1007/s44246-023-00037-5.
26 R. Guo, D. Li, C. Lv, Y. Wang, H. Zhang, Y. Xia, D. Yang and X. Zhao, *Electrochim. Acta*, 2019, **299**, 72–79, DOI: 10.1016/j.electacta.2019.01.011.
27 G. Jean and G. Bancroft, *Geochim. Cosmochim. Acta*, 1986, **50**(7), 1455–1463, DOI: 10.1016/0016-7037(86)90319-4.
28 K. Mainali, C. A. Mullen, M. I. Sarker, S. Haghighi Mood and M. Garcia-Perez, *Biomass Bioenergy*, 2024, **185**, 107221, DOI: 10.1016/j.biombioe.2024.107221.
29 S. Haghighi Mood, M. Ayiania, H. Cao, O. Marin-Flores, Y. J. Milan and M. Garcia-Perez, *Biomass Convers. Biorefin.*, 2024, **14**, 5923–5942, DOI: 10.1007/s13399-021-01404-1.
30 V. Budarin, J. H. Clark, J. J. Hardy, R. Luque, K. Milkowski, S. J. Tavener and A. J. Wilson, *Angew. Chem., Int. Ed.*, 2006, **45**, 3782–3786, DOI: 10.1002/anie.200600460.
31 H. Li, C. Li, V. L. Budarin, J. H. Clark, M. North, J. Wang and X. Wu, *Green Chem.*, 2022, **24**, 1545–1560, DOI: 10.1039/D1GC03715C.
32 D. Dai, Q. Ma, Y. Pei, Z. Zheng and L. Yuan, *Dalton Trans.*, 2018, **47**, 17421–17431, DOI: 10.1039/C8DT03803A.
33 M. N. Scheidema and P. Taskinen, *Ind. Eng. Chem. Res.*, 2011, **50**, 9550–9556, DOI: 10.1021/ie102554f.
34 Z. Liu, F. Li, Y. Miao, G. Zhang, Z. Pang, C. Zhang and X. Lin, *Sep. Purif. Technol.*, 2024, **340**, 126836, DOI: 10.1016/j.seppur.2024.126836.
35 X. Wang, Y. Yang, R. Wang, L. Li, X. Zhao and W. Zhang, *Langmuir*, 2022, **38**, 7280–7289, DOI: 10.1021/acs.langmuir.2c00805.
36 I. Barin, in *Thermochemical Data of Pure Substances*, ed. H. F. Ebel and C. Dyllick-Brenzinger, VCH, 1989, vol. 1 & 2.
37 D. Lei, S. Li, L. Gao, M. Hu, N. Chai and J. Fan, *Environ. Sci. Pollut. Res. Int.*, 2023, **30**, 115543–115555, DOI: 10.1007/s11356-023-30529-1.
38 S. Gulliani, M. Volpe, A. Messineo and R. Volpe, *RSC Sustainability*, 2023, **1**, 1085–1108, DOI: 10.1039/D3SU00034F.
39 S. A. Al-Saydeh, M. H. El-Naas and S. J. Zaidi, *J. Ind. Eng. Chem.*, 2017, **56**, 35–44, DOI: 10.1016/j.jiec.2017.07.026.
40 G. Nascimento, R. Souza, F. Fiore and A. Dantas de Jesus, *Clean. Eng. Technol.*, 2024, **21**, 100771, DOI: 10.1016/j.clet.2024.100771.
41 C. Campillo-Cora, A. Rodríguez-Seijo, P. Pérez-Rodríguez, D. Fernández-Calviño and V. Santás-Miguel, *Eur. J. Soil Biol.*, 2025, **124**, 103706, DOI: 10.1016/j.ejsobi.2024.103706.
42 S. Liu, Q. Sun, N. Xu, Y. Wang, Y. Li, J. Li, Z. Li, V. D. Rajput, T. Minkina, X. Kong, G. Li, Y. Lin, Y. Zhao and X. Duan, *Coord. Chem. Rev.*, 2025, **523**, 216268, DOI: 10.1016/j.ccr.2024.216268.
43 B. I. Musah, *Environ. Monit. Assess.*, 2024, **197**, 12, DOI: 10.1007/s10661-024-13490-5.
44 N. Garland, R. Gordon, C. McElroy, A. Parkin and D. J. Macquarrie, *ChemSusChem*, 2024, **17**, e202400015, DOI: 10.1002/cssc.202400015.
45 M. Ismail, A. Jobara, H. Bekouche, M. A. Allateef, M. A. B. Aissa and A. Modwi, *J. Mater. Sci.: Mater. Electron.*, 2022, **33**, 12500–12512, DOI: 10.1007/s10854-022-08207-8.
46 S. Kalam, S. A. Abu-Khamsin, M. S. Kamal and S. Patil, *ACS Omega*, 2021, **6**, 32342–32348, DOI: 10.1021/acsomega.1c04661.
47 N. Ayawei, A. N. Ebelegi and D. Wankasi, *J. Chem.*, 2017, **2017**, 1–11, DOI: 10.1155/2017/3039817.
48 J.-P. Simonin, *Chem. Eng. J.*, 2016, **300**, 254–263, DOI: 10.1016/j.cej.2016.04.079.
49 S. Ahmed, M. Badsha, A. Mahmood, A. Mushtaq and R. Sarfraz, *Int. J. Environ. Sci. Technol.*, 2025, **22**, 1609–1616, DOI: 10.1007/s13762-024-05741-2.
50 P. N. Amaniampong, Q. T. Trinh, J. J. Varghese, R. Bahling, S. Valange, S. H. Mushrif and F. Jérôme, *Green Chem.*, 2018, **20**, 2730–2741, DOI: 10.1039/c8gc00961a.
51 J. M. Aguirre, A. Gutiérrez and O. Giraldo, *J. Braz. Chem. Soc.*, 2011, **22**, 546–551, DOI: 10.1590/S0103-50532011000300019.
52 G. Di Leberto, F. Maleki and G. Pacchioni, *J. Phys. Chem. C*, 2022, **126**, 10216–10223, DOI: 10.1021/acs.jpcc.2c02289.
53 S. Ardizzone, C. L. Bianchi, M. Fadoni and B. Vercelli, *Appl. Surf. Sci.*, 1997, **119**, 253–259, DOI: 10.1016/S0169-4332(97)00180-3.
54 S. Anandan, J. J. Wu and M. Ashokkumar, *ChemPhysChem*, 2015, **16**, 3389–3391, DOI: 10.1002/cphc.201500629.
55 Q. T. Trinh, K. Bhola, P. N. Amaniampong, F. Jérôme and S. H. Mushrif, *J. Phys. Chem. C*, 2018, **122**(39), 22397–22406.
56 D. G. Castner, K. Hinds and D. W. Grainger, *Langmuir*, 1996, **12**, 5083–5086, DOI: 10.1021/la960465w.